

# Discovering Subsolar Metallicity Brown Dwarf Candidates in the Small Magellanic Cloud

Peter Zeidler<sup>1</sup> , Elena Sabbi<sup>2,3,4</sup> , Antonella Nota<sup>4,5</sup> , Elena Manjavacas<sup>1,6</sup> , Olivia C. Jones<sup>7</sup> , and Camilla Pacifici<sup>4</sup>   
<sup>1</sup>AURA for the European Space Agency (ESA), ESA Office, Space Telescope Science Institute, 3700 San Martin Drive, Baltimore, MD 21218, USA; [zeidler@stsci.edu](mailto:zeidler@stsci.edu)

<sup>2</sup> Gemini Observatory/NSFs NOIRLab, 950 N. Cherry Avenue, Tucson, AZ 85719, USA

<sup>3</sup> Steward Observatory, University of Arizona, Tucson, AZ 85721, USA

<sup>4</sup> Space Telescope Science Institute, 3700 San Martin Drive, Baltimore, MD 21218, USA

<sup>5</sup> The International Space Science Institute, Hallerstrasse 6, 3012 Bern, Switzerland

<sup>6</sup> Department of Physics and Astronomy, Johns Hopkins University, 3400 N. Charles Street, Baltimore, MD 21218, USA

<sup>7</sup> UK Astronomy Technology Centre, Royal Observatory, Blackford Hill, Edinburgh, EH9 3HJ, UK

Received 2024 April 24; revised 2024 August 27; accepted 2024 August 29; published 2024 October 23

## Abstract

We present the discovery of the first rich population of brown dwarf candidates (cBD) at subsolar metallicity, observed by JWST outside the Milky Way (MW) in the young SMC star cluster NGC 602. Located in the Small Magellanic Cloud (SMC) “wing,” in a very low-density environment ( $1.3 \text{ cm}^{-3}$ ) and at subsolar metallicity, NGC 602 is very young, with an age of 2–3 Myr. The low stellar density in this star cluster together with JWST NIRCam images in eight filters allowed us to individually resolve and derive accurate photometric measurements for 64 candidate BDs with masses ranging from  $0.05$  to  $0.08 M_{\odot}$  or  $50$  to  $84 M_{\text{Jup}}$ , according to brown dwarf (BD) evolutionary models. This is the first detection of a young BD population outside the MW. Their spatial distribution indicates that they appear colocated with the pre-main-sequence stars. Although further detailed work is required to quantitatively derive the initial mass function and confirm the true nature of the cBD, this discovery is particularly relevant in the effort to refine our understanding of the subsolar mass function at very low metallicities and young ages.

*Unified Astronomy Thesaurus concepts:* Brown dwarfs (185); Small Magellanic Cloud (1468); Young star clusters (1833); James Webb Space Telescope (2291); Initial mass function (796)

## 1. Introduction

The shape of the mass function at substellar masses is still a topic of discussion (e.g., N. Bastian et al. 2010; M. Gennaro & M. Robberto 2020; T. S. Tanvir et al. 2022; J. D. Kirkpatrick et al. 2024, and references therein) that is being increasingly enriched especially by new infrared (IR) observations of star-forming regions (e.g., K. L. Luhman et al. 2024) obtained by the James Webb Space Telescope (JWST; J. P. Gardner et al. 2023). The power of JWST is the superb combination of increased resolution and sensitivity at wavelengths where the bulk of substellar emission is released. Existing IR surveys indicate that the shape of the substellar mass function is consistent among young clusters in the Milky Way (MW; e.g., K. Mužić et al. 2017; S. Pearson et al. 2021; M. Robberto et al. 2024), pointing to its uniformity. With JWST it is now finally possible to extend this analysis outside the MW to young clusters in nearby galaxies, such as the Magellanic Clouds, and test whether variations in metallicity, interstellar medium (ISM) density, or location within a galaxy can affect the IMF in the subsolar mass regime. Furthermore, we can test whether the substellar mass function is a continuation of the stellar mass function, as has been indicated by multiple MW surveys (e.g., S. S. R. Offner et al. 2014, and reference therein), but in an environment different to the solar neighborhood. In this case, these low-mass objects would form through the fragmentation and collapse of

giant molecular clouds (GMCs) like stars and originate from the smallest cores, in contrast to forming as low-mass companions in circumstellar disks of protostars and being subsequently ejected (e.g., K. L. Luhman 2012; N. Miret-Roig 2023, and references therein).

NGC 602, a young stellar cluster (YSC) located in the “wing” of the Small Magellanic Cloud (SMC), is an ideal target for such an in-depth JWST study. NGC 602 is located at a distance of  $\sim 61$  kpc (R. W. Hilditch et al. 2005) and is the central YSC of the H II region N90 (K. G. Henize 1956). The SMC “wing” is characterized by a very low ISM density ( $1.3 \text{ cm}^{-3}$ ; J. Roman-Duval et al. 2014); still, NGC 602 formed  $\sim 2$ – $3$  Myr ago with a mass budget of  $M_{\star} = 1.6 \times 10^3 M_{\odot}$  (M. Cignoni et al. 2009), which makes it comparable to well-studied MW YSCs such as the Orion Nebula Cluster (M. Robberto et al. 2013; M. Gennaro & M. Robberto 2020) or Trumpler 14 in the Carina Nebula (M. Reiter & R. J. Parker 2019). L. Nigra et al. (2008) examined possible formation scenarios and concluded that NGC 602 was created by the collision and interaction of H I shell structures. The collision scenario was further refined by Y. Fukui et al. (2021), who found three velocity components in new H I data from the Galactic Australian Square Kilometre Array Pathfinder. Two of those components have a  $\sim 20 \text{ km s}^{-1}$  velocity separation and a displacement of 147 pc, indicating that two clouds might have collided and triggered the formation of NGC 602 and the more than 11 O and B stars in its center.

L. R. Carlson et al. (2007) used the Hubble Space Telescope (HST; GO-10248, P.I. A. Nota) to study NGC 602 in the optical to derive the upper mass function of the central cluster (mostly O and B stars), but prompted by the discovery of an



Original content from this work may be used under the terms of the [Creative Commons Attribution 4.0 licence](https://creativecommons.org/licenses/by/4.0/). Any further distribution of this work must maintain attribution to the author(s) and the title of the work, journal citation and DOI.



**Figure 1.** NGC 602 observed with NIRCam. This image highlights the cluster stars, the young YSOs embedded in the surrounding gas and dust ridges, as well as the gas and dust itself, while also showing the significant contamination by background galaxies and SMC field stars. This image is a composite of the F115W+F140M +F150W (blue), F210M (cyan), F277W (green), F335M (yellow), F356W (orange), and F480M+MIRI-F1000W (red) filters. While the wideband filters show the stellar and galaxy continua, the F335M highlights the  $3.3 \mu\text{m}$  PAH emission. This image is zoomed in on the star cluster. The full data (see Figure 5) cover an area of  $3 \times 5.8 \text{ arcmin}^2$ , of which  $\sim 2/3$  is occupied by NGC 602 and its surrounding H II region. North is up and east to the left.

extensive pre-main-sequence (PMS) population<sup>8</sup> in the mass range  $0.6\text{--}3 M_{\odot}$ , they combined the HST observations with Spitzer (GTO-125, P.I. G. Fazio). L. R. Carlson et al. (2007) then discovered a population of more than 40 embedded young stellar objects (YSOs)<sup>9</sup> of Class I to III, with masses between  $2.5$  and  $25.8 M_{\odot}$ , mostly concentrated along the dust ridges of NGC 602. From the spatial distribution of the YSOs, they concluded that the far-ultraviolet (FUV) fluxes of the central O and B stars are the drivers of star formation in the surrounding H II region. However, their analysis was limited by Spitzer's spatial resolution ( $1''\text{--}6''$ ), and it was not possible to match the Hubble and Spitzer data to optimum effectiveness.

Recently, using Atacama Large Millimeter/submillimeter Array high spatial resolution observations of the same region, T. J. O'Neill et al. (2022) found CO clumps spatially arranged along the NGC 602 dust ridges. They found that, in general, YSOs are embedded in the CO clumps, but there is no correlation between the age of the YSOs and their radial distance from the NGC 602 cluster. Therefore, they concluded that there is no strong evidence that NGC 602 has directly triggered star formation along the ridges, favoring instead a sequential star formation scenario.

<sup>8</sup> Throughout this work we are using the term PMS star for those young objects that are concentrated in the cluster center, which have mostly cleared their circumstellar material, being left with a thin disk, and are  $2\text{--}3$  Myr old. For the  $\sim 20$  Myr old PMS stars (G. De Marchi et al. 2013), we use the term “old PMS population.”

<sup>9</sup> We use the term YSO for all young objects that are still embedded within gas and dust ridges surrounding NGC 602.

The SMC “wing” is at the boundary between the body of the SMC and the SMC Bridge, with the Bridge being, at least partially, a tidally stripped component extending toward the Large Magellanic Cloud (LMC; S. Rubele et al. 2015). For NGC 602, G. De Marchi et al. (2013) found a slightly higher metallicity value, yet we want to emphasize that this cluster is still representative of a subsolar metallicity regime and provides a good laboratory for studying the substellar mass function in a low-density, low-metallicity environment.

In Cycle 1 of the JWST mission, we were awarded NIRCam time (14.6 h, GO-2662, P.I.: P. Zeidler) to perform such a study of NGC 602. In this work, we present the first results from the analysis of the JWST NIRCam images of NGC 602 (see Figure 1), namely, the discovery of a previously unknown but rich population of substellar objects, brown dwarf candidates (cBDs), reaching down to  $\sim 50$  Jupiter masses.

## 2. Observation, Data Reduction, and Photometry

On 2023 April 25, we used JWST/NIRCam (M. J. Rieke et al. 2023) to observe NGC 602 (GO-2662, P.I.: P. Zeidler) with four medium and four wideband filters: F115W, F140M, F150W, F210M, F277W, F335M, F356W, and F480M, mapping an area of  $3 \times 5.8 \text{ arcmin}^2$ , of which  $\sim 2/3$  is covered by NGC 602 and its surrounding H II region. For all filters, we applied a standard three-point subpixel dither pattern to optimally sample the point-spread function (PSF). This is critical, especially at short wavelengths where NIRCam is

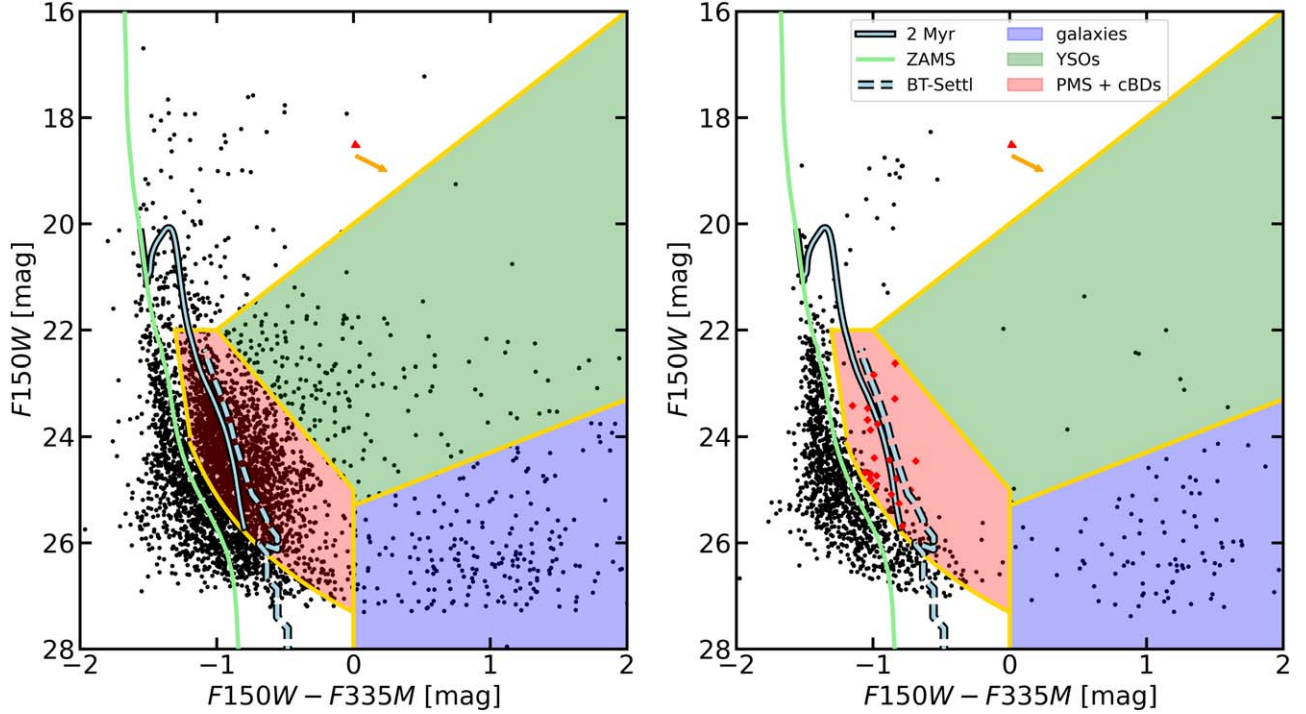


**Figure 2.** The  $F150W - F335M$  vs.  $F150W$  CMD of the cluster region (left) and CF (right). The red arrow indicates the reddening vector for  $A_V = 0.25$  mag, while the orange arrow indicates an assumed  $A_V = 1.0$  mag. The ZAMS is represented as a green line, and we show the 2 Myr MESA isochrones in blue using an LMC metallicity with a low-mass limit of  $0.01 M_\odot$ . The dashed blue line shows the BT-Settl BD isochrone, which includes the BD regime. The yellow lines represent the limits used to identify the lower-mass PMS population (shaded in red), the cYSO region (shaded in green), and the region mostly affected by background galaxies (shaded in blue). The red diamonds are those objects in the CF that are classified as PMS after applying all selection criteria.

undersampled. We substituted the primary dithers with a specially designed  $2 \times 2$  mosaic, with which we reached a total exposure time of 1288.4 s (per filter) in the cluster center and a control field (CF) outside the cluster region. The observations were comprised of 12 individual exposures using one integration with five groups and the BRIGHT1 readout pattern resulting in a single integration exposure time of 107.37 s.

We reduced the data using the JWST data reduction pipeline (v1.12.5; H. Bushouse et al. 2023), executing all standard pipeline steps for an optimal parameter selection. All observations are aligned to the Gaia DR3 astrometric solution (A. G. Brown et al. 2021) using the “The JWST HST Alignment Tool” (A. Rest et al. 2023) and are  $1/f$ -noise corrected<sup>10</sup> using `imageoverf.py` developed by Chris Willott.<sup>11</sup>

For our photometry, we used Starbug II (C. Nally 2023), a PSF photometry package specifically developed for complex and crowded regions, which has been applied successfully to similar data sets (e.g., C. Nally 2023; O. C. Jones et al. 2023; L. Lenkić et al. 2024). In order to be included in the final catalog, a source must be detected in at least two adjacent wideband filters,<sup>12</sup> and the magnitude uncertainty must be less than 0.75 mag, which was chosen to retain faint sources. All of the photometry is reported in the AB magnitude system to only use internal calibration properties<sup>13</sup> and to avoid applying the

measured, Sirius-based conversion to Vega zero points (K. D. Gordon et al. 2022).

Our final catalog consists of a total of 16,113 point sources with  $F115W$ : 13,391;  $F140M$ : 14,572;  $F150W$ : 13,397;  $F210M$ : 10,921;  $F277W$ : 12,859;  $F335M$ : 12,192;  $F356W$ : 14,261; and  $F480M$ : 8430 individual sources. All catalogs were plotted over the individual images and inspected by eye to ensure their reliability.

An in-depth description of the data, the data reduction, and all its products will be provided in future work (P. Zeidler et al. 2024, in preparation).

Throughout this work we use a distance modulus of 18.9 mag, representing the generally accepted distance for NGC 602 of 60.9 kpc (R. W. Hilditch et al. 2005). We applied the K. D. Gordon et al. (2023) extinction law, specifically developed for JWST in the near-IR, to all isochrones. We use a total visual extinction of  $A_V = 0.25$  and  $E(B - V) = 0.08$  (L. R. Carlson et al. 2007), which is lower than the mean gas and dust attenuation toward the SMC ( $A_V = 0.41 \pm 0.09$  mag; P. Yanchulova Merica-Jones et al. 2021) due to NGC 602 location in the SMC “wing.”

### 3. Identifying cBDs

To identify the young cluster population and separate it from possible contaminants like unresolved background galaxies and field stars, we applied selection cuts in various color-magnitude diagrams (CMDs; see Figures 2 and 3). Especially, we used the filters that highlight spectral energy distribution (SED) features unique to young stars and their remaining circumstellar material (e.g., the  $3.3 \mu\text{m}$  PAH region;  $F335M$ ) to facilitate the identification of protostars, YSOs, and cBDs. The low gas and dust attenuation results in a significant number of

<sup>10</sup> <https://jwst-docs.stsci.edu/jwst-near-infrared-camera/nircam-instrumentation/nircam-detector-overview/nircam-detector-performance>

<sup>11</sup> <https://github.com/chriswillott/jwst>

<sup>12</sup> Due to the same exposure time for all filters, the wideband photometry goes slightly deeper than the medium bands.

<sup>13</sup> <https://jwst-docs.stsci.edu/jwst-near-infrared-camera/nircam-performance/nircam-absolute-flux-calibration-and-zero-points>

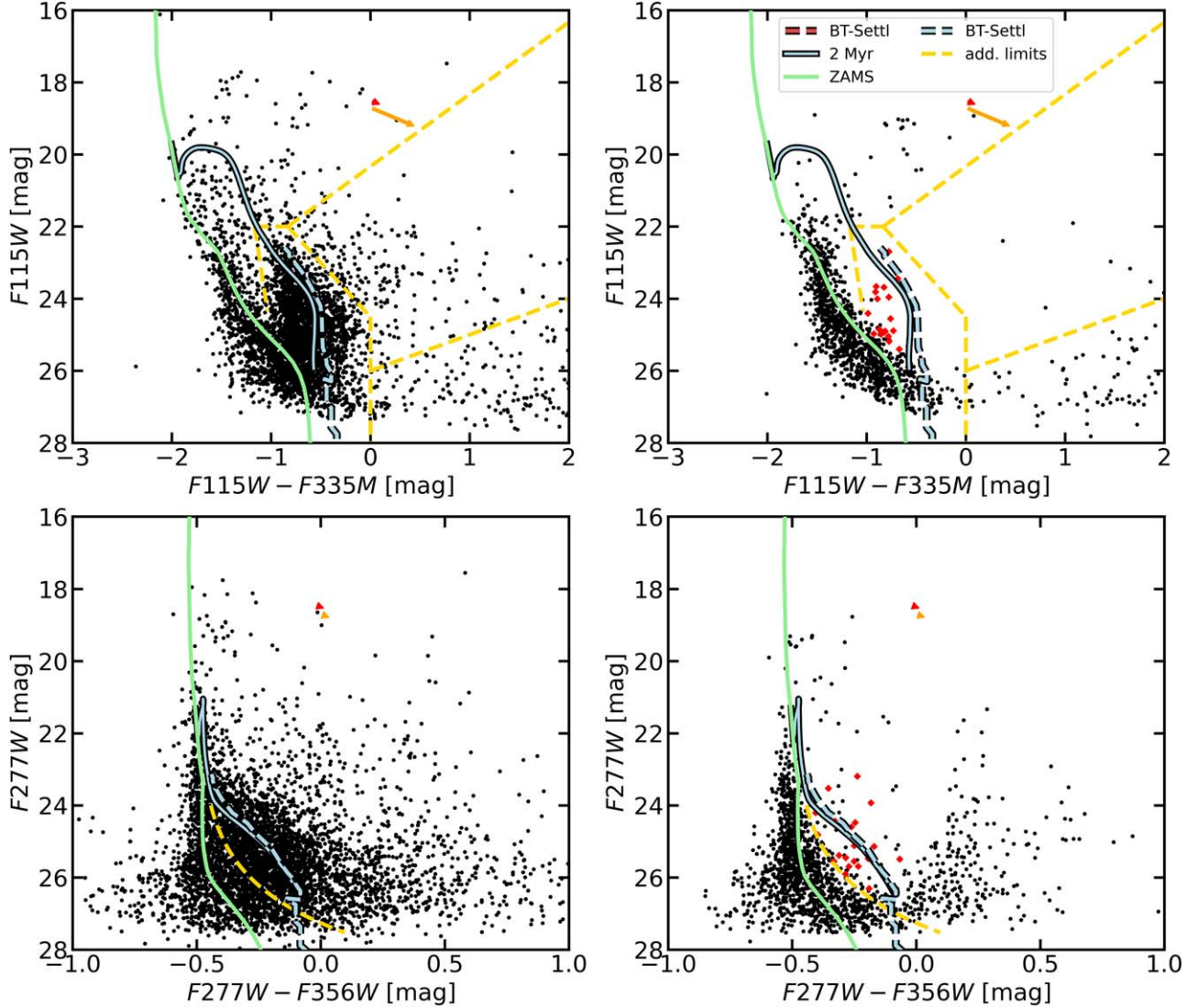


**Figure 3.** The  $F115W - F335M$  vs.  $F115W$  (top) and  $F277W - F356W$  vs.  $F277W$  (bottom), similar to Figure 2, showing the additional limits utilized to obtain a cleaner sample of PMS and BD candidates.

contaminants from unresolved galaxies (see Figure 1). Their locus in CMDs is similar to the young low-mass cluster population (PMS stars, YSOs). Thus it is particularly challenging to isolate the cluster members. A detailed analysis of the contaminants is presented in Section 3.3.

### 3.1. Selecting the Stellar Populations toward NGC 602

To select the young cluster population, we utilized the  $F115W - F335M$  versus  $F115W$ ,  $F150W - F335M$  versus  $F150W$ , and  $F277W - F356W$  versus  $F277W$  CMDs in combination with MESA isochrones and evolutionary tracks (A. Dotter 2016; J. Choi et al. 2016). We chose this particular set of CMDs since the young stellar population is well separated from the older main-sequence (MS) stars. We notice that for isochrones produced with a  $Z \sim 1/2 Z_{\odot}$  metallicity, typical for the LMC, this is a better fit than the  $Z_{\text{SMC}} \sim 1/5 Z_{\odot}$  metallicity (S. C. Russell & M. A. Dopita 1992; J.-K. Lee et al. 2005). Although deficits in the underlying models for the relatively new JWST filters cannot be excluded and will be investigated in the future, a possible deviation from the standard SMC metallicity was already indicated in G. De

Marchi et al. (2013). Furthermore, C. J. Evans et al. (2012) also found a significant [N/H] abundance enrichment compared to the average SMC value using Very Large Telescope FLAMES spectra of SK183 the most massive star in NGC 602. Recent studies (P. Massana et al. 2022; C. E. Murray et al. 2024) show that the ISM at the location of NGC 602 in the SMC wing may have been affected by interactions with the LMC, further explaining these findings. To validate our choice of stellar isochrones, we tested them against the Padova PARSEC tracks (CMD 3.7; A. Bressan et al. 2012; Y. Chen et al. 2014) as well as the BHAC15 tracks (I. Baraffe et al. 2015), which yielded comparable results.

We used and combined various cuts and limits within the  $F150W - F335M$  versus  $F150W$  CMD (Figure 2) to select three main groups: PMS stars, candidate YSOs (cYSOs), and background galaxies. To establish the selection criteria we used two circular regions ( $r = 1$  arcmin), one centered on the cluster (cluster region; R.A. =  $01^{\text{h}}29^{\text{m}}29\text{.790}$ , decl. =  $-73^{\circ}33^{\text{m}}34\text{.11}$ ) and the other located well outside the surrounding H II region west of NGC 602 (R. A. =  $01^{\text{h}}28^{\text{m}}47\text{.848}$ , decl. =  $-73^{\circ}33^{\text{m}}09\text{.93}$ ), which acts as our CF. We plotted all point sources within each

region in separate panels in Figure 2 to limit the confusion in each plot. The cluster population is shown in the left panel and the CF on the right. In each CMD we overplotted the MESA zero-age main sequence (ZAMS; green line) and the 2 Myr stellar isochrone (blue line), while the 2 Myr BT-Settl brown dwarf (BD) isochrone (F. Allard et al. 2011, 2012) is marked as a dashed blue line to guide the reader’s eyes. The two arrows indicate the established mean reddening vector toward NGC 602 of  $A_V = 0.25$  mag and an assumed more extreme reddening of  $A_V = 1.0$  mag. Based on these CMDs as well as the location of the isochrones and evolutionary tracks we selected three main groups:

1. The lower-mass PMS, whose circumstellar material is mostly present in a thin circumstellar disk (shaded in red).
2. cYSOs, young stars that are still embedded in the natal H II region and thus are embedded in a significant amount of circumstellar material (shaded in green).
3. Unresolved background galaxies and very embedded YSOs (shaded in blue).

The used cuts and limits are indicated by the yellow lines in Figure 2. In order to obtain a cleaner sample we furthermore utilized the F115W–F335M versus F115W and F277W–F356W versus F277W CMDs (see Figure 3) by introducing additional limits (dashed yellow lines). The red diamonds in Figures 2 and 3 are those objects in the CF that are classified as PMS after applying all selection criteria and thus are possible contaminants. In Section 3.3 we will present a detailed contamination analysis. All our selection criteria are consistent with the publications of O. C. Jones et al. (2022), L. Lenkić et al. (2024), and N. Habel et al. (2024).

### 3.2. The Cluster Populations of NGC 602

In Figure 4 we plot our full point-source catalog (gray dots) using the F115W–F335M versus F115W, F150W–F335M versus F150W, and F277W–F356W versus F277W CMDs. We include the ZAMS (black line), the 1, 2, and 3 Myr isochrones (in red, blue, and yellow, respectively), as well as a 4.2 Gyr isochrone that represents the stellar SMC field population. The selected PMS stars are highlighted with red dots, which are well represented by the chosen isochrones in agreement with the previous optical identification and classifications (M. Cignoni et al. 2009; L. R. Carlson et al. 2011; T. J. O’Neill et al. 2022). In green we show the cYSOs.

Most notably, a sequence of faint, red sources (marked as yellow diamonds) continues well below the  $0.1 M_\odot$  PMS stars. These sources are considerably redder than the MS field stars and have magnitudes and colors consistent with those predicted by the BT-Settl (F. Allard et al. 2011, 2012; green), ATMO2020 (M. W. Phillips et al. 2020; orange), and BHAC15 (I. Baraffe et al. 2015; cyan) BD evolutionary models. Hereafter, we will call these 64 objects cBDs. Due to intracluster reddening it is possible that some of these cBDs are indeed reddened PMS stars or even reddened MS stars. In Section 3.3 we will present a detailed contamination analysis.

While the BT-Settl isochrones are available at lower than solar metallicity ( $[Fe/H] = -0.5$ ), the ATMO2020 and BHAC15 isochrones are only available for solar metallicity. Despite this difference, all three models are in agreement with each other and show a good continuation of the stellar isochrones toward lower masses, below the hydrogen-burning limit.

In total, we select 2078 PMS stars, 205 cYSOs, and 64 cBDs within our survey area. Based on the BT-Settl and BHAC15 isochrones, the possible temperature range for these BDs is 2800–3100 K. In contrast to MS stars, BDs do not have enough mass to fuse hydrogen; thus, since they are born, they cool down with time (A. Burrows et al. 1997; I. Baraffe et al. 2003). As a result, for a given luminosity and temperature, their masses are a function of age. Assuming an age of 2 Myr these BDs have masses between  $0.048$  and  $0.08 M_\odot$  or  $50$  and  $84 M_{Jup}$ . As Z. H. Zhang et al. (2017) show, the mass at which hydrogen fusion sets in increases with decreasing metallicity; thus, for  $[Fe/H] = -0.5$  we can assume  $0.08 M_\odot$  instead of the typical  $0.075 M_\odot$  limit. The inferred BD masses from the BT-Settl and BHAC15 models agree well with each other. This is also true for the ATMO2020 model despite the note of M. W. Phillips et al. (2020) that this model misses some sources of opacities, which specifically affects objects younger than 10 Myr and  $M > 0.015 M_\odot$ , and therefore this model should be treated with caution.

### 3.3. The Contaminating Sources

In the following we carefully analyze possible contaminants that can mimic a BD signal in our CMDs, such as unresolved background galaxies and highly reddened cluster and SMC field stars. We applied two different methods:

1. We are applying the same selection criteria to only the CF, which provides us with an upper limit of possible background sources that occupy the same region in the CMD as PMS stars, YSOs, and BDs.
2. We use the CF CMD with which we statistically decontaminate the selected cluster region CMD. Assuming that the real background population is uniformly distributed over such a relatively small region within the SMC, we can estimate how many MS stars are possibly located within the PMS, YSO, and BD region caused by reddening.

#### 3.3.1. The Field Population Mimicking PMS, YSOs, and BDs

The F115W–F335M versus F115W and F150W–F335M versus F150W CMDs of the CF show that, while the majority of these sources populate the MS, there are a few objects (red diamonds in Figures 2 and 3) within the YSO and PMS region that do not get removed applying the PMS selection criteria. Given the low extinction toward the SMC we assume that reddening in the CF is negligible and that the number of YSOs, PMS stars, and BDs in the SMC field is very small. Thus, based on this analysis the field contaminants (e.g., unresolved background galaxies or evolved stars) yield 2.10% and 0.56% for PMS stars and cYSO, respectively.

#### 3.3.2. Reddened Field and Older Cluster Population

While the above estimate assumes no extinction, this is of course not true for the cluster region, where background objects from the SMC field and bluer background galaxies might be reddened due to the gas and dust of the H II region. Therefore, we statistically subtract the CF from the cluster region. We randomly “match” a cluster star and a field star (within an uncertainty-dependent color-magnitude radius) and remove the object from both the CF and cluster region CMDs. To bootstrap our result we repeated the above procedure 100 times. Since we expect a similar number of SMC field stars in the cluster region

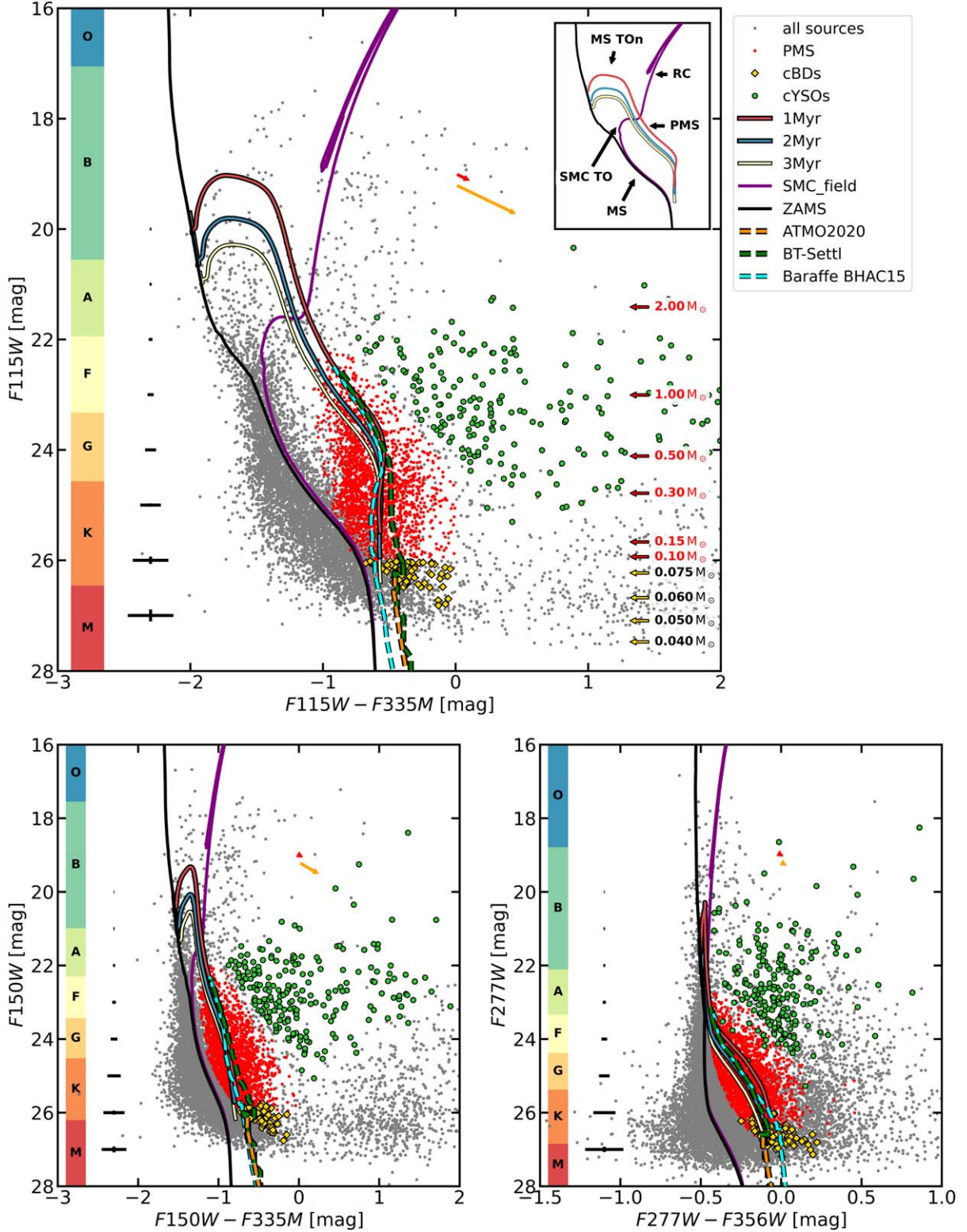


**Figure 4.** The  $F115W - F335M$  vs.  $F115W$  (top),  $F150W - F335M$  vs.  $F150W$  (bottom left), and  $F277W - F356W$  vs.  $F277W$  (bottom right) CMDs. The inlay on top shows the main features of the CMDs: MS, PMS, red clump (RC), MS turn-on (MS TOn), and SMC turnoff (SMC TO). The red arrow indicates the reddening vector for  $A_V = 0.25$  mag, while the orange arrow indicates an assumed  $A_V = 1.0$  mag. Gray points correspond to all point sources of our catalog. In red we show PMS stars, in green cYSO, and the yellow diamonds represent our discovered cBD population. On the left side of each plot, we show the mean photometric errors in bins of 1 mag and the spectral types for MS stars. The ZAMS is represented as a black line, and we show the 1, 2, and 3 Myr isochrones in red, blue, and yellow, respectively, using the MESA isochrones and stellar tracks for an LMC metallicity with a low-mass limit of  $0.1 M_\odot$ . The purple track represents the 4.2 Gyr SMC field population. The dashed lines show BD isochrones: BT-Settl (green), ATMO2020 (orange), and BHAC15 (cyan). On the right we show the stellar (red numbers) and BD masses (yellow numbers) corresponding to the 2 Myr isochrones.

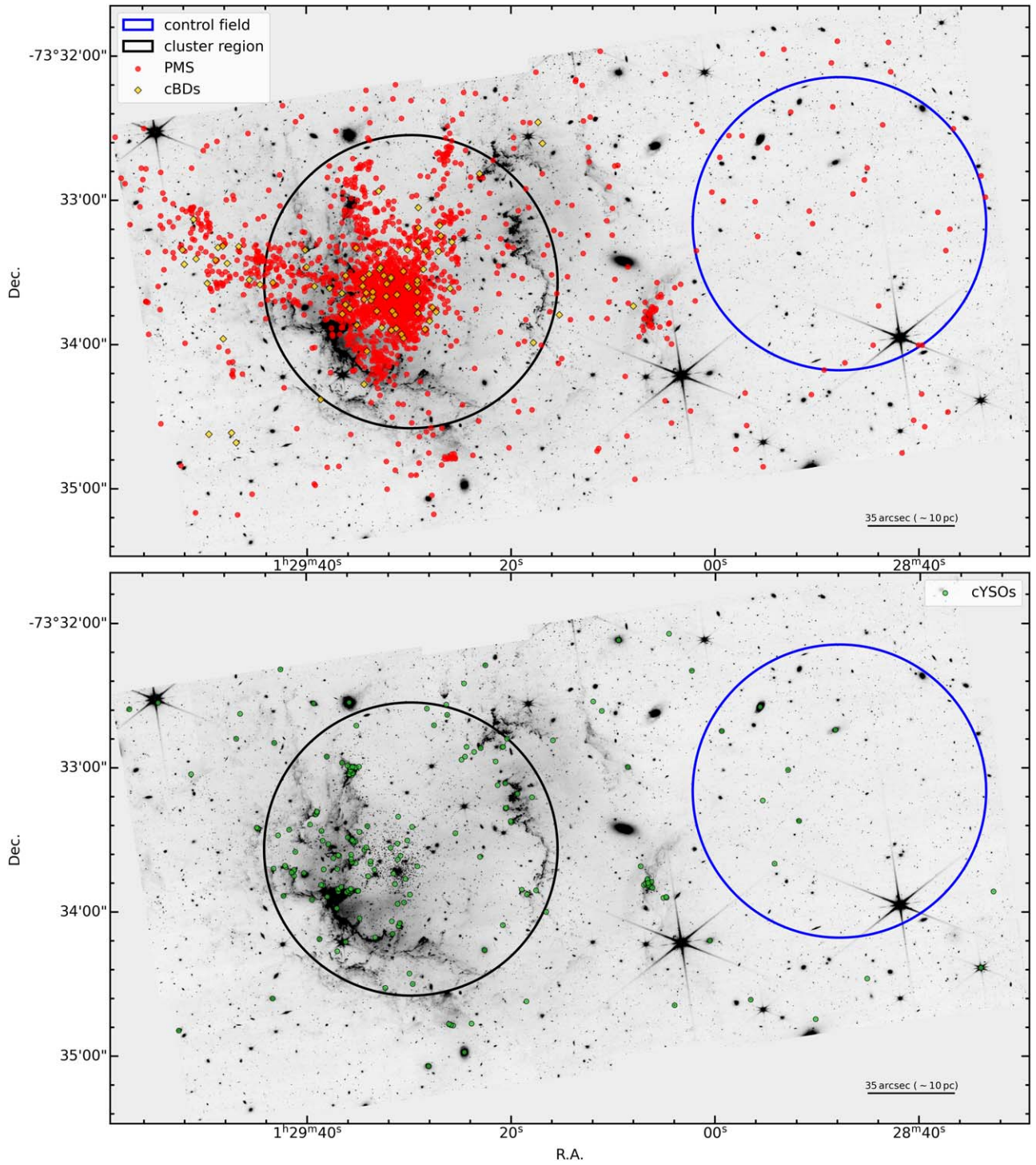


**Figure 5.** The spatial distribution of the PMS stars and cBDs (upper panel) and the cYSOs (lower panel). The PMS stars and the cBDs follow the same spatial distribution, while the cYSOs are mainly located on the gas and dust ridges. The blue circle marks the CF used to estimate the contamination from the SMC field stars and the background galaxies. The black circle marks the equally sized cluster region. The underlying image is the F277W filter. North is up, and east is to the left.

and the CF, any source that remains in the CF CMD after the removal is “missing” in the cluster region. These “missing” objects are most likely reddened and thus shifted to redder colors and fainter magnitudes not having a match between both CMDs. Based on the rather conservative assumption that all of these objects end up in the PMS and BD region of the CMD we estimate an upper contamination fraction of  $5.0 \pm 0.4\%$ .

YSOs, especially Class I and II, can have intrinsic color excesses large enough that some might be located in the galaxy region of the CMDs. Using SED fitting in a future work will allow us to separate these two populations.

G. De Marchi et al. (2013) found an older ( $>20$  Myr) PMS population in NGC 602. The locus of these old PMS stars is close to or overlaps with the ZAMS in our CMDs, so this

population does not need to be treated as an additional contaminant.

In conclusion at most  $7.2 \pm 0.7\%$  of all PMS stars and cBDs and  $5.9 \pm 0.3\%$  of all cYSOs can be caused by extinction or field stars and background galaxies mimicking similar colors and magnitudes within our CMDs. This translates to a total of 150 PMSs, 5 cBDs, and 12 cYSOs.

#### 4. The Spatial Distribution of the Cluster Population

Analyzing the spatial distribution of the young cluster population, we find that the PMS stars and cBDs appear colocated and follow the same spatial distribution.

The PMS stars are concentrated toward the cluster center (red dots in Figure 5) in agreement with the findings of L. R. Carlson et al. (2007, 2011) and G. De Marchi et al. (2013) using optical HST data. We find three stream-like features to the north and northeast of the cluster. These “streams” appear to trace the gaps in the gas and dust ridges (see Figure 1), similar to what was recently found in NGC 346, another SMC star-forming region (E. Sabbi et al. 2022; P. Zeidler et al. 2022). This also suggests these stars may have cleared the material of the parental GMC either during their formation or due to feedback processes (or a combination of the two). These features are (barely) visible in the optical data presented by M. Cignoni et al. (2009) and T. J. O’Neill et al. (2022).

The cYSOs on the other hand follow a different spatial distribution, which is supported by a  $p$ -value of  $1.84 \times 10^{-16}$  using a two-sample Kolmogorov–Smirnov test (KS test). The majority of cYSOs are located on the gas and dust ridges, where we expect to find most of the currently ongoing star formation (L. R. Carlson et al. 2011; T. J. O’Neill et al. 2022). The fewer cYSOs in the cluster center can be explained by gas depletion. In other words, there is a reduced ongoing star formation rate due to the effect of the high FUV fluxes and stellar winds emitted by the massive O and B stars.

The cBDs (yellow diamonds in Figure 5) follow a very similar spatial distribution as the PMS stars ( $p = 0.08$ ), including their location in the three stream-like features, which is confirmed by the normalized cumulative radial distribution relative to the cluster center (see Figure 6). From this we conclude that the cBDs could have formed synchronously with the PMS stars. The absence of BDs in the gas ridges is likely a consequence of detection bias in these dense regions with a high background rather than an indication that no new BDs are forming. Furthermore, even if we detect more embedded BDs, these would be located in the same region as the background galaxies or MS stars in our CMDs, thus not allowing a clean selection.

#### 5. Implications for the Stellar Mass Function

The ability to accurately predict the shape of the initial mass function (IMF) remains a major challenge for star formation theories (e.g., N. Bastian et al. 2010). Generally, the IMF consists of a broad peak centered around the characteristic or mean mass  $m_c$ , which is assumed to be around  $0.2\text{--}0.3 M_\odot$ . A power-law tail extending toward higher masses is often described by an E. E. Salpeter (1955) IMF. All stars below  $1 M_\odot$  comprise  $\sim 70\%$  of the stellar mass budget; thus, even small deviations in  $m_c$  have significant effects on the evolution of a star cluster. Studies suggest that stellar radiation feedback can influence  $m_c$ , where low-mass young stars radiate due to accretion, raising the

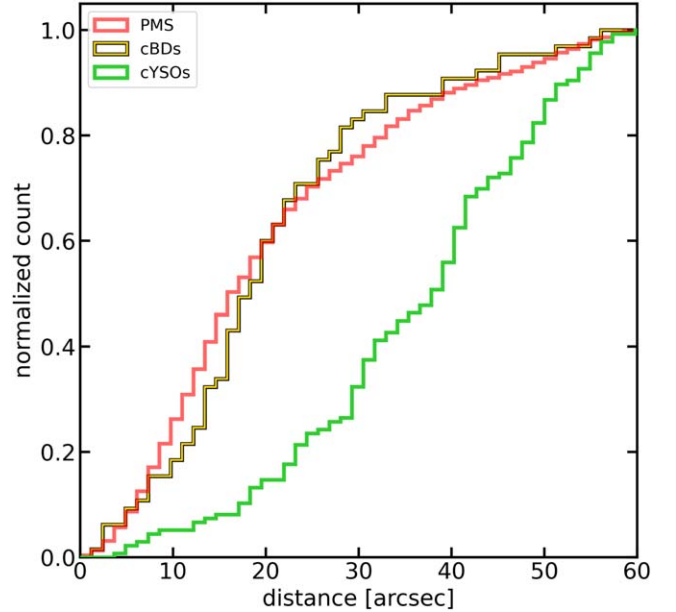


**Figure 6.** The normalized cumulative radial distribution of the PMS stars (red), cYSOs (green), and cBDs (yellow) within the inner 60'' from the cluster center. The PMS stars and BDs are similarly distributed, confirmed by the KS test. The cYSOs are less concentrated in the cluster center.

surrounding gas temperature and thus the Jeans mass. This strongly suppresses fragmentation, which in turn suppresses the formation of low-mass objects (e.g., M. R. Krumholz 2006; S. S. Mathew & C. Federrath 2020, 2021; T. S. Tanvir et al. 2022; M. R. Krumholz et al. 2023). Protostellar jet feedback may have a similar effect, and indeed D. Guszejnov et al. (2016) showed that there appears to be a trend that  $m_c$  shifts to higher masses with higher initial temperatures, which is the case in low-metallicity environments such as the SMC.

Based on the results presented in Section 3.2 our data set reaches well below the characteristic mass. Extensive artificial star tests are necessary to determine and correct for the position, filter, magnitude, and color-dependent incompleteness of our data set, yet this already shows that we will be able to determine the substellar mass function in a young star cluster outside the MW planned for future work. This will either confirm that the BD formation is truly a continuation of the stellar mass function (e.g., P. Kroupa 2001; G. Chabrier 2003), as expected from solar neighborhood studies, or whether there is a transition region where BDs start to form dominantly through the fragmentation of circumstellar disks (e.g., M. Marks et al. 2017).

#### 6. Summary and Conclusions

In this work we present the detection of the first subsolar metallicity ( $Z \approx 1/5\text{--}1/2 Z_\odot$ ) cBDs outside the MW. Using our JWST/NIRCam photometry of the young SMC star cluster NGC 602, in combination with the F115W–F335M versus F115W, F150W–F335M versus F150W, and F277W–F356W versus F277W CMDs and evolutionary models of both young stars (MESA, A. Dotter 2016; J. Choi et al. 2016) and BDs (BT-Settl, ATMO2020, BHAC15 F. Allard et al. 2011, 2012; I. Baraffe et al. 2015; M. W. Phillips et al. 2020), we found the following:

1. A rich population of 64 cBDs with masses ranging from 0.05 to  $0.08 M_{\odot}$  or 50 to  $84 M_{\text{Jup}}$ .
2. A spatial distribution for the cBDs that indicates colocation with the young PMS stars throughout the cluster region, and thus both populations formed synchronously, suggesting continuation of the stellar mass function into the substellar mass regime, thus assuming a common origin.

One of the biggest challenges in studying the IMF below the hydrogen-burning limit is to accurately determine the masses of these substellar objects (e.g., K. L. Luhman 2012; N. Miret-Roig 2023). Compared to stars, objects without stable hydrogen fusion are on a continuous cooling sequence; hence, a spectral-type (effective temperature)-based mass can only be estimated with the knowledge of their ages and using evolutionary models for BDs. Based on the spatial colocation of the cBDs and the PMS stars (see Figures 5 and 6), we assume that our detected cBDs likely formed coevally with their stellar counterparts. This allows us to use the ages of the PMS stars in NGC 602, which formed between 2 and 3 Myr ago (determined through isochrone fitting; e.g., L. R. Carlson et al. 2007; M. Cignoni et al. 2009, and Figure 4).

The accurate selection of ages together with the superb sensitivity and calibration of JWST will allow us, in a forthcoming paper, to reliably study the substellar mass function, well below the turnover of the IMF. With this knowledge we can verify if the substellar IMF is a continuation of the stellar IMF and thus answer whether these objects likely form like stars by the fragmentation and collapse of GMCs or through the fragmentation of circumstellar disks, similar to planets (K. L. Luhman 2012; M. Marks et al. 2017). From this work, the colocation with the PMS (see Figure 5) suggests that the formation channel of the cBDs is the same as the one for their more massive stellar counterparts, as expected from solar neighborhood studies: the fragmentation and collapse of the GMC.

### Acknowledgments

We would like to thank Varun Bajaj for his support in aligning the NIRCam images to the Gaia DR3 reference frame. We also want to thank Connor Nally for his support in using Starbug II for our data set. OCJ has received funding from an STFC Webb fellowship. We thank the anonymous referee for the thorough and detailed report that helped to improve the results of this work. This work is based on observations made with the NASA/ESA/CSA James Webb Space Telescope. The data were obtained from the Mikulski Archive for Space Telescopes at the Space Telescope Science Institute, which is operated by the Association of Universities for Research in Astronomy, Inc., under NASA contract NAS 5-03127 for JWST. These observations are associated with program #2662.

The JWST data presented in this article were obtained from the Mikulski Archive for Space Telescopes (MAST) at the Space Telescope Science Institute. The specific observations analyzed can be accessed via doi:[10.17909/x2h4-kv56](https://doi.org/10.17909/x2h4-kv56).

Facility: JWST (NIRCam).

### ORCID iDs

Peter Zeidler <https://orcid.org/0000-0002-6091-7924>

Elena Sabbi <https://orcid.org/0000-0003-2954-7643>  
 Antonella Nota <https://orcid.org/0009-0007-8087-6975>  
 Elena Manjavacas <https://orcid.org/0000-0003-0192-6887>  
 Olivia C. Jones <https://orcid.org/0000-0003-4870-5547>  
 Camilla Pacifici <https://orcid.org/0000-0003-4196-0617>

### References

Allard, F., Homeier, D., & Freytag, B. 2011, in ASP Conf. Ser. 448, 16th Cambridge Workshop on Cool Stars, Stellar Systems, and the Sun (San Francisco, CA: ASP)

Allard, F., Homeier, D., & Freytag, B. 2012, *RSPTA*, 370, 2765

Baraffe, I., Chabrier, G., Barman, T. S., Allard, F., & Hauschildt, P. H. 2003, *A&A*, 402, 701

Baraffe, I., Homeier, D., Allard, F., & Chabrier, G. 2015, *A&A*, 577, A42

Bastian, N., Covey, K. R., & Meyer, M. R. 2010, *ARA&A*, 48, 339

Bressan, A., Marigo, P., Girardi, L., et al. 2012, *MNRAS*, 427, 127

Brown, A. G., Valenari, A., Prusti, T., et al. 2021, *A&A*, 649, A1

Burrows, A., Marley, M., Hubbard, W. B., et al. 1997, *ApJ*, 491, 856

Bushouse, H., Eisenhamer, J., Dencheva, N., et al. 2023, JWST Calibration Pipeline, v1.12.5, Zenodo, doi:[10.5281/zenodo.10022973](https://doi.org/10.5281/zenodo.10022973)

Carlson, L. R., Sabbi, E., Sirianni, M., et al. 2007, *ApJ*, 665, L109

Carlson, L. R., Sewilo, M., Meixner, M., et al. 2011, *ApJ*, 730, 22

Chabrier, G. 2003, *PASP*, 115, 763

Chen, Y., Girardi, L., Bressan, A., et al. 2014, *MNRAS*, 444, 2525

Choi, J., Dotter, A., Conroy, C., et al. 2016, *ApJ*, 823, 102

Cignoni, M., Sabbi, E., Nota, A., et al. 2009, *AJ*, 137, 3668

De Marchi, G., Beccari, G., & Panagia, N. 2013, *ApJ*, 775, 68

Dotter, A. 2016, *ApJS*, 222, 8

Evans, C. J., Hainich, R., Oskinova, L. M., et al. 2012, *ApJ*, 753, 173

Fukui, Y., Habe, A., Inoue, T., Enokiya, R., & Tachihara, K. 2021, *PASJ*, 73, S1

Gardner, J. P., Mather, J. C., Abbott, R., et al. 2023, *PASP*, 135, 24

Gennaro, M., & Robberto, M. 2020, *ApJ*, 896, 80

Gordon, K. D., Bohlin, R., Sloan, G. C., et al. 2022, *AJ*, 163, 267

Gordon, K. D., Clayton, G. C., Decler, M., et al. 2023, *ApJ*, 950, 86

Guszejnov, D., Krumholz, M. R., & Hopkins, P. F. 2016, *MNRAS*, 458, 673

Habel, N., Nally, C., Lenkić, L. L., et al. 2024, *ApJ*, 971, 108

Henize, K. G. 1956, *ApJS*, 2, 315

Hilditch, R. W., Howarth, I. D., & Harries, T. J. 2005, *MNRAS*, 357, 304

Jones, O. C., Nally, C., Habel, N., et al. 2023, *NatAs*, 7, 694

Jones, O. C., Reiter, M., Sanchez-Janssen, R., et al. 2022, *MNRAS*, 517, 1518

Kirkpatrick, J. D., Marocco, F., Gelino, C. R., et al. 2024, *ApJS*, 271, 55

Kroupa, P. 2001, *MNRAS*, 322, 231

Krumholz, M. R. 2006, *ApJ*, 641, L45

Krumholz, M. R., Crocker, R. M., & Offner, S. S. R. 2023, *MNRAS*, 520, 5126

Lee, J.-K., Rolleston, W. R. J., Dufton, P. L., & Ryans, R. S. I. 2005, *A&A*, 429, 1025

Lenkić, L., Nally, C., & Jones, O. C. 2024, *ApJ*, 967, 110

Luhman, K. L. 2012, *ARA&A*, 50, 65

Luhman, K. L., Alves de Oliveira, C., Baraffe, I., et al. 2024, *AJ*, 167, 19

Marks, M., Martín, E. L., Béjar, V. J., et al. 2017, *A&A*, 605, 11

Massana, P., Ruiz-Lara, T., Noël, N. E. D., et al. 2022, *MNRAS*, 513, L40

Mathew, S. S., & Federrath, C. 2020, *MNRAS*, 496, 5201

Mathew, S. S., & Federrath, C. 2021, *MNRAS*, 507, 2448

Miret-Roig, N. 2023, *Ap&SS*, 368, 17

Murray, C. E., Hasselquist, S., Peek, J. E. G., et al. 2024, *ApJ*, 962, 120

Mužić, K., Schödel, R., Scholz, A., et al. 2017, *MNRAS*, 471, 3699

Nally, C., 2023 StarbugII: JWST PSF photometry for crowded fields, Astrophysics Source Code Library, ascl:[2309.012](https://doi.org/10.26435/ascl.2309.012)

Nigra, L., Gallagher, J. S., Smith, L. J., et al. 2008, *PASP*, 120, 972

Offner, S. S. R., Clark, P. C., Hennebelle, P., et al. 2014, in Protostars and Planets VI, ed. H. Beuther (Tucson, AZ: Univ. Arizona Press)

O'Neill, T. J., Indebetouw, R., Sandstrom, K., et al. 2022, *ApJ*, 938, 82

Pearson, S., Scholz, A., Teixeira, P. S., Muzic, K., & Almendros-Abad, V. 2021, *MNRAS*, 507, 4074

Phillips, M. W., Tremblin, P., Baraffe, I., et al. 2020, *A&A*, 637, A38

Reiter, M., & Parker, R. J. 2019, *MNRAS*, 486, 4354

Rest, A., Pierel, J., Correnti, M., et al. 2023 The JWST HST Alignment Tool (JHAT), v2, zenodo, doi:[10.5281/zenodo.7892935](https://doi.org/10.5281/zenodo.7892935)

Rieke, M. J., Kelly, D. M., Misselt, K., et al. 2023, *PASP*, 135, 1044

Robberto, M., Gennaro, M., Da Rio, N., et al. 2024, *ApJ*, **960**, 49  
Robberto, M., Soderblom, D. R., Bergeron, E., et al. 2013, *ApJS*, **207**, 10  
Roman-Duval, J., Gordon, K. D., Meixner, M., et al. 2014, *ApJ*, **797**, 86  
Rubele, S., Girardi, L., Kerber, L., et al. 2015, *MNRAS*, **449**, 639  
Russell, S. C., & Dopita, M. A. 1992, *ApJ*, **384**, 508  
Sabbi, E., Zeidler, P., Marel, R. P. V. D., et al. 2022, *ApJ*, **936**, 135  
Salpeter, E. E. 1955, *ApJ*, **121**, 161  
Tanvir, T. S., Krumholz, M. R., & Federrath, C. 2022, *MNRAS*, **516**, 5712  
Yanchulova Merica-Jones, P., Sandstrom, K. M., Johnson, L. C., et al. 2021, *ApJ*, **907**, 50  
Zeidler, P., Sabbi, E., & Nota, A. 2022, *ApJ*, **936**, 136  
Zhang, Z. H., Homeier, D., Pinfield, D. J., et al. 2017, *MNRAS*, **468**, 261